

# Dual-Mode Infrared Absorption by Segregating Dopants within Plasmonic Semiconductor Nanocrystals

Stephen L. Gibbs, Christopher Dean, Joey Saad, Bharat Tandon, Corey M. Staller, Ankit Agrawal, and Delia J. Milliron\*

Cite This: *Nano Lett.* 2020, 20, 7498–7505

Read Online

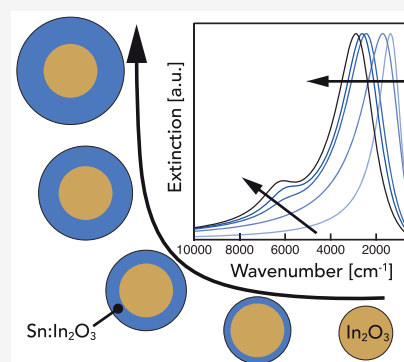
ACCESS |

Metrics & More

Article Recommendations

Supporting Information

**ABSTRACT:** When aliovalent dopants are sufficiently segregated to the core or near the surface of semiconductor nanocrystals, charge carriers donated by the dopants are also segregated to the core or near the surface, respectively. In Sn-doped indium oxide nanocrystals, we find that this contrast in free charge carrier concentration creates a core and shell with differing dielectric properties and results in two distinctly observable plasmonic extinction peaks. The trends in this dual-mode optical response with shell growth differ from core/shell nanoparticles composed of traditional plasmonic metals such as Au and Ag. We developed a model employing a core/shell effective medium approximation that can fit the dual-mode spectra and explain the trends in the extinction response. Lastly, we show that dopant segregation can improve sensitivity of plasmon spectra to changes in refractive index of the surrounding environment.



**KEYWORDS:** colloidal nanoparticles, localized surface plasmon resonance, effective medium, dielectric function, sensor

## INTRODUCTION

Plasmonic nanoparticles efficiently collect incident light and confine it to nanoscale volumes, which can drive enhanced electric fields,<sup>1–3</sup> localized heating,<sup>4,5</sup> and hot electron transfer.<sup>6–8</sup> Degenerately doped semiconductor nanocrystals (NCs) have proven to be efficient infrared (IR) plasmonic materials due to their intrinsically low plasmon damping and their low and easily tunable charge carrier concentration.<sup>9,10</sup> N-type semiconductors are classified as degenerate when the Fermi level rises above the conduction band minimum, leading to metallic conductivity and plasmonic optical response. The plasmonic response of doped semiconductor NCs of various sizes, shapes, and compositions has been well-studied,<sup>11–13</sup> but the distribution of dopants within a NC can also tune the optical behavior.<sup>14,15</sup> With the recent advent of slow-addition synthetic techniques for doped metal oxide NCs, we have greater control over the intra-NC radial doping profile than ever before.<sup>14,16,17</sup> This control elucidated that deliberately segregating aliovalent dopants to the surface (core) also segregates the majority of the charge-compensating free carriers derived from those dopants to the surface (core).<sup>18,19</sup> The potential established by space-charge buildup at the interface of the doped and undoped regions prevents charge carriers from distributing homogeneously throughout the nanocrystal. In other words, an inhomogeneous doping profile leads to an inhomogeneous charge carrier profile, even within a single nanocrystal. Leveraging this knowledge, the conductivity of NC films has been improved by segregating dopants near the NC surface.<sup>18</sup> Motivated by these results, we

sought to understand how engineering the intra-NC carrier concentration profile through dopant segregation impacts the plasmonic response.

Plasmonic structures with radially inhomogeneous compositions have already been employed to tune the optical response for traditional plasmonic materials such as Au and Ag. Most notably, silica@Au (core@shell) nanoshells were synthesized to bring the localized surface plasmon resonance (LSPR) peak of Au from the visible to the near-IR therapeutic window, enabling the demonstration of photothermal therapy in animal tissue.<sup>4</sup> Beyond shifting the peak extinction to lower energy, fundamental studies uncovered a dual-mode extinction spectrum from silica@Au nanoshells. More recently, bimetallic core@shell nanoparticles were synthesized and also exhibited dual-mode extinction.<sup>20–22</sup> These distinct modes arise because, unlike a homogeneous sphere, the core and shell are distinguishable due to the abrupt change in composition and dielectric properties at the core/shell boundary. Two surfaces emerge that can support plasmonic modes: the core/shell boundary and the nanoparticle outer surface.<sup>23,24</sup> In a similar way, herein we prove that the segregation of dopants, and

Received: July 20, 2020

Revised: September 7, 2020

Published: September 22, 2020



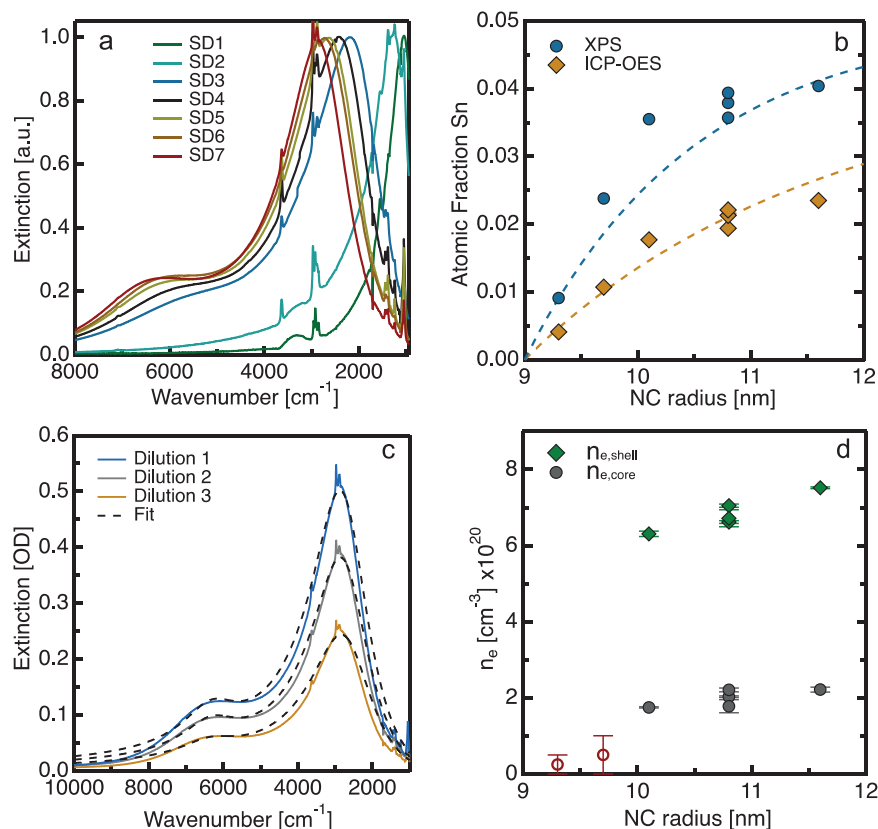


**Figure 1.** Experimental trends in shell-doped NCs. (a) Normalized experimental extinction spectra for the shell-doped series. (b) ICP-OES and XPS quantification of atom % Sn for each sample. Dashed lines indicate theoretical values based on measured STEM diameters and a photoelectron escape depth 1.5 nm. (c) Fits to spectra of SD7 at three NC concentrations. (d) Carrier concentration values for the core and the shell extracted by fitting to the core/shell MG-EMA model. Red, hollow circles indicate samples that were fit to a uniform dielectric function, not a core/shell effective medium approximation. Error bars represent the standard deviation in fit results when fitting the optical response of three independently prepared dispersions of varying NC concentration.

therefore charge carriers, within metal oxide nanocrystals creates an epitaxial core/shell boundary that promotes a dual-mode plasmonic response. The observed trends in the plasmonic extinction spectrum differ from those seen in silica@Au and bimetallic core@shell nanoparticles due to unique considerations of doped semiconductor NCs including dopant activation and charge carrier diffusion.

Specifically, we investigate the effect of intra-NC radial dopant distribution on the optical response of tin-doped indium oxide (ITO) NCs. We use this material as a model system for degenerately doped metal oxides because it is an industrially relevant transparent conductive oxide and colloidal synthesis of both undoped indium oxide (IO) and ITO NCs is well-developed.<sup>16,17</sup> We synthesize two series, one with an undoped core and a doped shell of increasing thickness and another with a doped core and an undoped shell of increasing thickness. We observe a dual-mode plasmonic extinction response in both cases. After building a model that accounts for a radially nonuniform intra-NC charge carrier profile, we were able to reliably fit all collected spectra and extract electronic parameters that explain the evolution of the dual-mode spectra. We show that dopant segregation expands the synthetic tunability of the optical response and enhances sensitivity to the surroundings when compared to uniform doping. Lastly, these findings may resolve the origin of anomalous, asymmetric lineshapes of plasmonic-doped metal

oxide NCs that have gone unexplained in previous literature.<sup>14,25,26</sup>

## ■ SHELL-DOPED SERIES

Radial segregation of dopants has been shown to influence peak position, peak width, and peak asymmetry,<sup>14,15,25,27</sup> but no published studies of dopant-segregated NCs have identified dual-mode extinction spectra. In the shell-doped (SD) series, aliquots were taken as a shell of 5 atom % Sn was epitaxially grown over an undoped IO core as detailed in Supporting Information (SI) Text 1. During shell growth we observe the appearance and progressive strengthening of a secondary extinction mode at substantially higher energy than the main LSPR peak (Figure 1a). Relatively weak peaks between 2000 and 4000 cm<sup>-1</sup> are assigned to molecular vibrational modes for species on or near the NC surface (Figure S1).

X-ray photoelectron spectroscopy (XPS) and inductively coupled plasma-optical emission spectroscopy (ICP-OES) quantified near-surface Sn and overall Sn, respectively. The data confirms that the dopants are indeed segregated to the surface with near-surface Sn concentration exceeding the overall Sn concentration by a factor of 2 on average for all samples (Figure 1b). In fact, our experimental results match very well with the theoretically calculated values for both XPS and ICP-OES (dashed lines). To calculate these theoretical values, we used the diameters measured using scanning transmission electron microscopy (STEM) and approximated

Table 1. Experimentally Measured Properties of Shell-Doped Samples

sample	radius $\pm 1\sigma$ [nm]	shell thickness $\pm 1\sigma$ [nm]	$F_{v,\text{core}} \pm 1\sigma$	atom % Sn by ICP-OES $\pm 1\sigma$	atom % Sn by XPS
SD0	9.0 $\pm$ 0.7	0	1		
SD1	9.3 $\pm$ 0.7	0.3 $\pm$ 0.9	0.92 $\pm$ 0.28	0.41 $\pm$ 0.01	0.9
SD2	9.7 $\pm$ 0.7	0.7 $\pm$ 1.0	0.79 $\pm$ 0.24	1.07 $\pm$ 0.03	2.4
SD3	10.1 $\pm$ 0.6	1.1 $\pm$ 0.9	0.71 $\pm$ 0.19	1.77 $\pm$ 0.07	3.6
SD4	10.8 $\pm$ 1.0	1.9 $\pm$ 1.2	0.57 $\pm$ 0.20	1.94 $\pm$ 0.05	3.6
SD5	10.8 $\pm$ 0.8	1.8 $\pm$ 1.0	0.58 $\pm$ 0.17	2.13 $\pm$ 0.03	3.8
SD6	10.8 $\pm$ 0.6	1.8 $\pm$ 0.9	0.58 $\pm$ 0.15	2.21 $\pm$ 0.03	3.9
SD7	11.6 $\pm$ 0.7	2.6 $\pm$ 1.0	0.47 $\pm$ 0.13	2.35 $\pm$ 0.04	4.0

the photoelectron escape depth as 1.5 nm.<sup>28</sup> Sample details are reported in Table 1 with radius, shell thickness, and core volume fraction ( $F_{v,\text{core}}$ ) calculated from particle sizes acquired through STEM (Figure S2).

The difference in Sn content measured by the two techniques suggests that the change in Sn concentration is abrupt between core and shell, more than reported previously.<sup>14</sup> In that case, a temporally varying precursor composition was slowly injected in a single-pot reaction to control the radial Sn doping profile but without the extra step of isolating and purifying the undoped cores before starting shell growth, as is done in this work. We conclude that the isolation of NC cores as an intermediate product is an important step in sharpening the dopant profile at the core/shell interface while still maintaining epitaxial growth of single crystal nanoparticles.<sup>16,18</sup>

A sharper dopant profile creates a steeper step in the electrostatic potential and a stronger segregation of charge carriers to the doped region.<sup>18,19</sup> This sharp delineation is reminiscent of the aforementioned silica@Au nanoshells and bimetallic core@shell nanoparticles that also supported two distinct modes. However, the evolution of the two modes is not what we expected based on the plasmon hybridization theory.<sup>23</sup> According to this theory, as the thickness of the metallic shell grows, the higher energy mode should red-shift and the lower energy mode should blue-shift, bringing them closer together. We observe a blue-shift in both modes (Figure 1a). This discrepancy is not surprising because we know that the carrier concentration in ITO NCs increases with size due to increased dopant activation.<sup>15,29</sup> Dopant activation is the ratio between the free electron concentration,  $n_e$ , and the dopant concentration. Near-surface dopants are more likely to be “inactive”, meaning they are charge-compensated by a mechanism other than with free charge carriers. The fraction of near-surface Sn drops with doped shell growth due to diminishing surface area to volume ratio, causing dopant activation and  $n_e$  to increase. No analogous change in  $n_e$  is expected for growth of Au or Ag shells. We sought to fit the spectra to a model that could account for changing dielectric properties of the core and shell.

### EXTRACTING ELECTRONIC PARAMETERS

We built a model to fit our experimental spectra to extract electronic parameters and examine their evolution with shell thickness (SI Text 4). Using a least-squares fit function in MATLAB, we fit for plasma frequency,  $\omega_p$ , and damping,  $\Gamma$ , in both the core and the shell. The polarizability of a spherical particle with a core and shell having different dielectric properties can be well-approximated using an electromagnetic mixing formula known as the Maxwell-Garnett effective medium approximation (MG-EMA),<sup>30</sup> described briefly in SI

Text 2. Also, because the carrier profile is expected to deviate slightly from the doping profile due to diffusion of free electrons, we fit for the volume fraction of the core instead of using  $F_{v,\text{core}}$  values calculated from STEM diameters. The decreasing trend in  $F_{v,\text{core}}$  with shell growth determined by fitting the LSPR spectra agrees with the STEM-derived values (Figure S6). As well, the fitted values consistently fall above the STEM-derived values for the shell-doped nanocrystals. We attribute this offset to diffusion of carriers from the higher  $n_e$  shell to the lower  $n_e$  core, causing the shell volume to shrink. While there is some diffusion of carriers across the core/shell boundary, the majority of carriers derived from Sn n-type donors are still localized to the shell. The physics governing this diffusion are directly analogous to an n/n+ junction wherein free electrons redistribute locally in the near-junction space-charge region.<sup>18</sup>

Our model reliably fit experimental data for all samples and produced consistent fit results for independently prepared dispersions of varying NC concentration (Figures 1c and S3). Details of the fitting procedure are reported in SI Text 3. The fit results are reported in Table S1 and plotted in Figures S6 and S7. We note that samples SD1 and SD2 show only unimodal extinction, and so these spectra were fit with the traditional Drude model for particles with a uniform dielectric function. The very low energy peaks are indicative of low  $n_e$  throughout the entire NC volume (Figure 1d). For samples SD3–SD7, the trends in  $n_e$  clarify the underlying physico-chemical changes leading to the emergence and progressive blue-shift in the secondary mode. As the ITO shell grows in thickness,  $n_e$  in the shell also increases. As expected, this upward trend results from increasing activation of Sn for thicker shells where a smaller fraction of the dopants are near-surface. For the same reason, uniformly doped 5 atom % Sn ITO NCs were previously found to have increasing  $n_e$  up to a radius of 12 nm.<sup>29</sup> The carrier concentration in the undoped core is also impacted by growth of an ITO shell, surpassing a value of  $2 \times 10^{20} \text{ cm}^{-3}$  or about three times the  $n_e$  that has been reported for IO NCs with no shell.<sup>29</sup> We understand this elevated  $n_e$  to be due to diffusion of electrons from the high carrier concentration shell into the core, the same phenomenon driving the difference between STEM-derived and fit-derived values for  $F_{v,\text{core}}$ . Increasing dopant activation and carrier diffusion from the shell to the core explain the discrepancy of our results with the plasmon hybridization theory used for Ag and Au core@shell particles.

### CORE-DOPED SERIES

For the core-doped (CD) series, an undoped IO shell was grown around a 5 atom % ITO core (Figure S4). XPS and ICP-OES data once again confirm that the dopants are well-segregated and this time to the core. Near-surface Sn

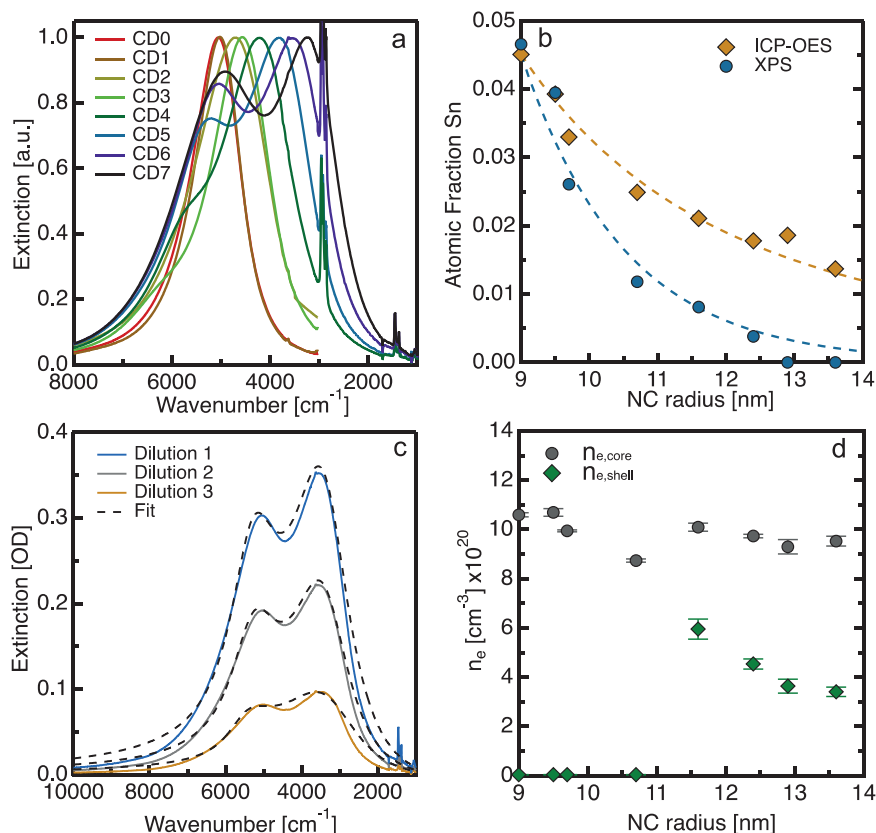


**Figure 2.** Experimental trends in core-doped NCs. (a) Normalized experimental extinction spectra for the core-doped series. (b) ICP-OES and XPS quantification of atom % Sn for each sample in the CD series. Dashed lines indicate theoretical values based on measured STEM diameters, a photoelectron escape depth 1.5 nm, and growth of an undoped shell. (c) Fits to spectra of CD6 at three NC concentrations. (d) Carrier concentration values for the core and the shell extracted by fitting to the core/shell MG-EMA model. Error bars represent the standard deviation in fit results when fitting the optical response of three independently prepared dispersions of varying NC concentration.

**Table 2. Experimentally Measured Properties of Core-Doped Samples**

sample	radius $\pm 1\sigma$ [nm]	shell thickness $\pm 1\sigma$ [nm]	$F_{v,core} \pm 1\sigma$	atom % Sn by ICP-OES $\pm 1\sigma$	atom % Sn by XPS
CD0	9.0 $\pm$ 1.1	0	1	4.51 $\pm$ 0.09	4.7
CD1	9.5 $\pm$ 0.9	0.6 $\pm$ 1.4	0.83 $\pm$ 0.39	3.93 $\pm$ 0.26	4.0
CD2	9.7 $\pm$ 1.0	0.7 $\pm$ 1.5	0.79 $\pm$ 0.38	3.30 $\pm$ 0.14	2.6
CD3	10. $\pm$ 1.1	1.8 $\pm$ 1.6	0.58 $\pm$ 0.28	2.49 $\pm$ 0.17	1.2
CD4	11.6 $\pm$ 0.9	2.7 $\pm$ 1.4	0.46 $\pm$ 0.20	2.11 $\pm$ 0.19	0.8
CD5	12.4 $\pm$ 1.0	3.4 $\pm$ 1.5	0.38 $\pm$ 0.17	1.78 $\pm$ 0.07	0.4
CD6	12.9 $\pm$ 1.2	3.9 $\pm$ 1.6	0.34 $\pm$ 0.16	1.86 $\pm$ 0.37	~0
CD7	13.6 $\pm$ 0.8	4.7 $\pm$ 1.4	0.29 $\pm$ 0.12	1.37 $\pm$ 0.06	~0

concentration is nearly identical to overall Sn for CD0, indicating uniform distribution of dopants in the ITO core, but as the IO shell thickness grows, values quickly diverge with near-surface Sn becoming undetectable for samples CD6 and CD7 (Figure 2b). Sample details are reported in Table 2.

Segregating dopants to the core will also concentrate the high  $n_e$  region to the core. Unlike a dielectric@metal particle, such as silica@Au, a metal@dielectric particle, such as Au@silica, does not produce a dual-mode extinction spectrum because there is only one surface to sustain LSPR. However, as noted for the SD series, the IO region contains a significant, albeit lower than the doped region, population of free electrons and so behaves like a metal, not an insulating dielectric. This metallicity explains the otherwise unexpected appearance and growth of a second mode with IO shell growth (Figure 2a). Simulations of bimetallic core@shell particles with the metal of higher  $\omega_p$  in the core (analogous to our CD series) have shown

that with increasing shell thickness, the high energy peak red-shifts and the low energy peak blue-shifts, bringing the peaks closer together. In our CD series, both modes red-shift with shell growth. Once again, the trend in our dual-mode spectra does not match that which is expected for a traditional metal core@shell particle. Using the same core@shell MG-EMA model as for the SD series, we sought to explain the discrepancy.

We achieved excellent fits to the experimental data (Figures 2c and S5) and extracted the trends in  $n_e$  for the core and shell (Figure 2d) as well as  $F_{v,core}$ . The fit results are reported in Table S2 and plotted in Figures S6 and S7. Consistent with the SD series, the fitted  $F_{v,core}$  values trend with the STEM-derived values. Also, the fitted  $F_{v,core}$  values consistently fall below the STEM-derived values, indicating carrier diffusion from the higher  $n_e$  core to the lower  $n_e$  shell.

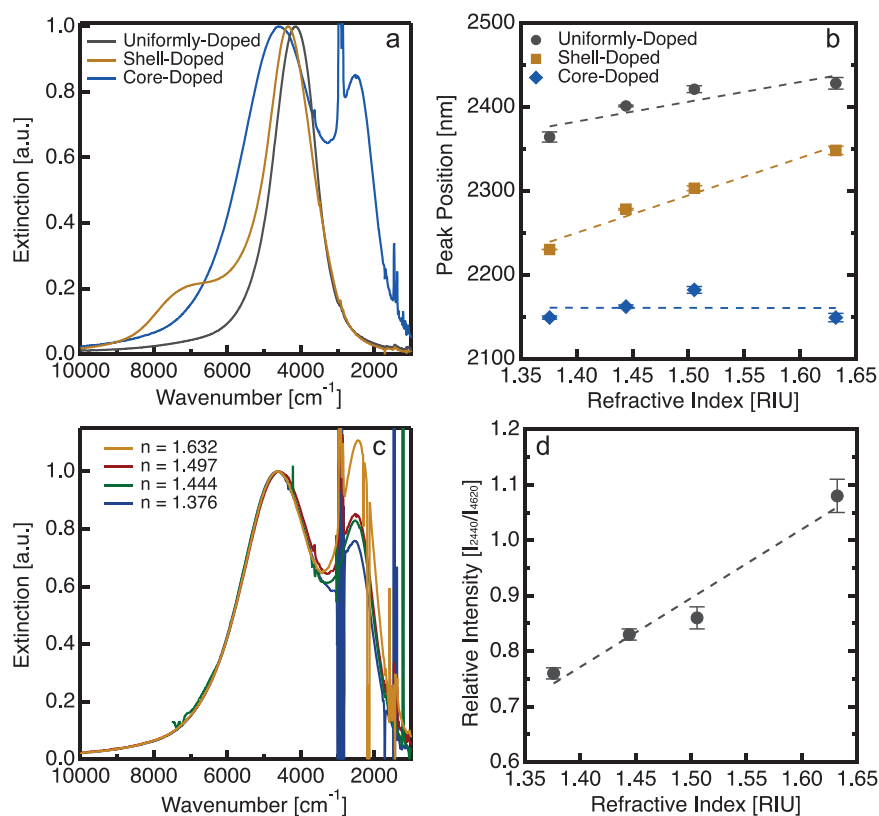


**Figure 3.** Dielectric sensitivity of dopant segregated NCs. (a) Normalized spectra for uniformly doped, shell-doped, and core-doped ITO NCs of similar  $\omega_{\text{LSPR}}$  dispersed in TCE. (b) Primary peak positions measured when each sample was dispersed in solvents of differing refractive index. (c) Core-doped spectra, normalized to the high energy mode, for NCs dispersed in all four solvents. (d) Relative intensity of the low energy mode with respect to the high energy mode as a function of refractive index for the core-doped sample shown in panel c. Error bars represent the standard deviation in peak position for three independently prepared dispersions of varying NC concentration. Dashed lines show linear fits.

**Table 3.** Comparison of the Dielectric Sensitivity of Nanocrystals with Differing Dopant Segregation

doping profile	core diameter $\pm 1\sigma$ [nm]	overall diameter $\pm 1\sigma$ [nm]	atom % Sn by ICP-OES $\pm 1\sigma$	atom % Sn by XPS	$S \pm \text{S.E.}^a$ [nm/RIU]	
					exp.	sim.
core-doped	$18.9 \pm 1.7$	$30.2 \pm 1.6$	$1.11 + 0.09$	$\sim 0$	$-2 \pm 101$	$155 \pm 14$
uniformly doped	n/a	$19.4 \pm 1.5$	$3.22 + 0.05$	4.5	$236 \pm 84$	$734 \pm 15$
shell-doped	$13.7 \pm 0.9$	$23.4 \pm 2.4$	$4.03 + 0.05$	6.4	$446 \pm 56$	$784 \pm 24$

<sup>a</sup>SE denotes the standard error in the slope of the linear regression

For samples CD0–CD3, the secondary mode is either absent or subtle, which our model attributes to a high  $n_e$  core and a shell nearly devoid of all free electrons, that is, a surface depletion layer.<sup>19,31</sup> However, when the IO shell reaches a critical thickness, around 2.7 nm, it contains a high enough  $n_e$  to support a strong secondary mode. Though  $n_e$  in the shell is higher than expected for undoped IO, the core  $n_e$  still well-exceeds it. As in the shell-doped NCs, the elevation of  $n_e$  in the IO region is understood to originate with diffusion of carriers from ITO. Carrier redistribution near the core/shell interface also explains the decrease in shell  $n_e$  with shell thickness for samples CD4–CD7: for thicker shells, the space-charge region near the IO/ITO junction comprises a smaller fraction of the shell volume, causing average  $n_e$  across the entire shell to decrease. Just as in the shell-doped case, it is necessary to account for the changing  $n_e$  profile with size to rationalize the evolution of the peaks.

In summary, while these experiments illustrated that sufficiently sharp dopant segregation can lead to dual-mode extinction in ITO NCs, we found that the interface still allows

some local redistribution of carriers that impacts the optical response. After extracting  $n_e$  from the fits, consideration of (1) near-surface dopant activation and (2) charge carrier diffusion at the IO/ITO interface were required to explain why the trends in peak position deviated from the established plasmon hybridization theory for metallic shells and bimetallic core@shell particles. As a first indication of how carrier segregation influences near-field optical properties of doped metal oxide NCs, we next investigated the response of their spectra to a changing dielectric environment.

## ■ DIELECTRIC SENSITIVITY

Plasmonic nanoparticles are commonly employed as sensors because the LSPR peak frequency,  $\omega_{\text{LSPR}}$ , shifts when the dielectric constant of the surroundings changes.<sup>1</sup> The magnitude of the peak shift is indicative of the strength of the enhanced electric field at the particle surface, that is, the near-field enhancement.<sup>32–34</sup> The strength of the electric field near the surface determines the effectiveness of many plasmonically powered processes. Principle among these are

surface-enhanced infrared spectroscopy (SEIRS),<sup>35–38</sup> enhanced light emission,<sup>2,39</sup> and interparticle coupling.<sup>40–42</sup>

For core@shell particles exhibiting dual-mode extinction (both dielectric@metal and metal@metal), the lower energy mode extends the majority of electric field enhancement outside the particle, whereas the higher energy mode confines much of the enhancement to the core/shell interface.<sup>20</sup> Therefore, we expect the lower energy modes to be more sensitive to changes in the surrounding refractive index. To compare dielectric sensitivity for samples of differing dopant distribution, we synthesized uniformly doped, shell-doped, and core-doped samples (Figure S8) with similar  $\omega_{\text{LSPR}}$  for the primary (more intense) peak (Figure 3a). We collected spectra for these samples dispersed in four different solvents (Figure S9). The sensitivity factor,  $S$ , (Table 3) is calculated by taking the slope of the line for peak wavelength as a function of solvent refractive index (Figure 3b).

Because the primary peak for the shell-doped sample is the lower energy mode and that of the core-doped sample is the higher energy mode, we expect the primary peak of the shell-doped particle to have higher refractive index sensitivity. This is indeed the case. The shell-doped sample is also more sensitive than the uniformly doped sample. We rationalize this difference based on the insulating effect of near-surface depletion.<sup>31,43</sup> While there is notable error in the linear fits to the data, the difference in slopes is large enough to conclude with 95% confidence that the difference in slopes, and therefore the sensitivity factors, is statistically significant (Table S3). Supporting this understanding, when we fit the optical response of the uniformly doped NCs in tetrachloroethylene (TCE) using the MG-EMA core@shell model, we find there is a shell nearly devoid of carriers (Table S4). This insulating effect is mitigated when a higher dopant concentration is segregated near the surface, thereby compressing the depletion layer thickness.<sup>18</sup>

We also fit the spectra for the core- and shell-doped samples dispersed in TCE. Using these extracted parameters, we simulated how the spectra are expected to shift in these different solvents (Figure S9). The simulated sensitivity values show the same trend as the experimental values; however, they are higher in all cases. This quantitative disagreement is likely due to the insulating effects of ligands<sup>44</sup> and the convoluting effects of ensemble heterogeneity,<sup>45</sup> neither of which is accounted for in the simulation.

From these results it can be inferred that at a given  $\omega_{\text{LSPR}}$ , shell-doped nanocrystals have the highest near-field enhancement at the surface and are best suited for coupling to vibrational or electronic transitions in nearby molecules or particles. When comparing peak sensitivity of the shell-doped and uniformly doped NCs to other plasmonic materials, we find it falls within the range observed for metallic nanoparticle ensemble measurements, which have ranged from 90 to 801 nm/RIU.<sup>1,46</sup> For these metals,  $\omega_{\text{LSPR}}$  ranges from the visible to the near-IR, with the lowest energy being 5570  $\text{cm}^{-1}$ . Whereas in this work, by using only ITO and maintaining spherical NCs under 30 nm in diameter, we have shown tunability in peak position from 6000 to 1000  $\text{cm}^{-1}$ , emphasizing the utility of doped metal oxide NCs in the near to mid-IR.

The sensitivity of the secondary (lower intensity) modes of the core- and shell-doped samples also matches the expectation based on enhanced electric field distribution in metallic core@shell particles. The higher energy mode in the shell-doped sample does not change significantly with surrounding

refractive index (Figure S9), while the lower energy mode in the core-doped sample appreciably changes intensity in comparison to the primary mode (Figure 3c). Modulation in relative peak intensity is useful for ratiometric sensing, wherein the relative peak intensities at two wavelengths are compared to monitor the surroundings. These sensors can be advantageous over single-mode sensors because they are internally referenced and thus less susceptible to noise from the environment.<sup>47–49</sup> Their sensitivity can be quantified by measuring the ratio of peak intensities versus refractive index (Figure 3d). In this case, our simulation again matched the trends in the experimental spectra (Figures 3d and S9); however, the sensitivity for our experiment (1.2) exceeded that of the simulation (0.35). We hypothesize the quantitative disagreement results from an increase in shell  $n_e$  with rising dielectric of the solvent. Prior work reported that increasing the dielectric constant of the surroundings can lower the ionization energy of defects, increasing  $n_e$ .<sup>50</sup>

## CONCLUSION

Engineering dopant distribution within doped metal oxide NCs changes the intra-NC charge carrier profile and the corresponding optical response. Varying the thickness of epitaxially grown shells, we observed the evolution of dual-mode IR extinction due to intra-NC dopant segregation. After fitting spectra with a MG-EMA core@shell model, the extracted  $n_e$  profile informed us that dopant activation and carrier diffusion, two factors unique to doped semiconductor NCs, explain the deviation in trends from metallic core@shell particles. This fitting method is not only applicable to ITO but can be used for any plasmonic semiconductor NC with defects segregated to a core or shell, both extrinsic and intrinsic defects. While the defects are placed deliberately in our system, for a self-doped material, such as metal oxides with oxygen vacancies or copper chalcogenides with cation vacancies, a nonuniform spatial distribution of defects would likely produce a nonuniform charge carrier profile and altered optical and electronic behavior. We suspect that the appearance of anomalous secondary modes and asymmetric lineshapes in recent literature may be due to unrecognized intra-NC dopant segregation.<sup>14,25,26</sup>

But more than simply changing the spectral line shape, segregation of dopants creates NCs that are optically and electronically inhomogeneous on an ultrafine length scale and all within a single crystal. The optical and electronic inhomogeneity investigated here must be considered in doped semiconductor NC analysis to accurately interpret their measured properties and to fully maximize their potential. For example, the ability to establish an intra-NC dielectric gradient even at relatively low doping levels makes intra-NC dopant placement an enticing opportunity for deep sub-wavelength confinement, an exciting prospect for infrared waveguiding.<sup>51,52</sup> Segregating charge carriers to the surface creates an IR plasmonic nanoantenna with strong near-field enhancement, an ideal candidate for SEIRS. This could also prove useful for plasmon-enhanced photocatalysis<sup>6,53–56</sup> wherein photon absorption promotes an energetic distribution of hot charge carriers that can be transferred to catalyze reactions. These hot carriers typically equilibrate with the lattice on picosecond time scales,<sup>57,58</sup> so surface segregation will reduce the carrier diffusion length to the catalytic surface. These potential applications merit continued exploration of dopant-segregated semiconductor NCs.

## ■ ASSOCIATED CONTENT

### Supporting Information

The Supporting Information is available free of charge at <https://pubs.acs.org/doi/10.1021/acs.nanolett.0c02992>.

Synthetic protocol, equipment and characterization technique specifications, bond vibrational mode assignments, STEM, discussion of effective medium theory, fitting plots and results for shell-doped and core-doped series, fitting plots and simulations for dielectric sensitivity samples, constraints for fit parameters, and MATLAB code (PDF)

## ■ AUTHOR INFORMATION

### Corresponding Author

**Delia J. Milliron** – McKetta Department of Chemical Engineering, University of Texas at Austin, Austin, Texas 78712, United States; [orcid.org/0000-0002-8737-451X](https://orcid.org/0000-0002-8737-451X); Phone: (512)232-5702; Email: [milliron@che.utexas.edu](mailto:milliron@che.utexas.edu)

### Authors

**Stephen L. Gibbs** – McKetta Department of Chemical Engineering, University of Texas at Austin, Austin, Texas 78712, United States; [orcid.org/0000-0003-2533-0957](https://orcid.org/0000-0003-2533-0957)

**Christopher Dean** – McKetta Department of Chemical Engineering, University of Texas at Austin, Austin, Texas 78712, United States

**Joey Saad** – McKetta Department of Chemical Engineering, University of Texas at Austin, Austin, Texas 78712, United States

**Bharat Tandon** – McKetta Department of Chemical Engineering, University of Texas at Austin, Austin, Texas 78712, United States; [orcid.org/0000-0003-1108-9859](https://orcid.org/0000-0003-1108-9859)

**Corey M. Staller** – McKetta Department of Chemical Engineering, University of Texas at Austin, Austin, Texas 78712, United States; [orcid.org/0000-0001-8665-2840](https://orcid.org/0000-0001-8665-2840)

**Ankit Agrawal** – The Molecular Foundry, Berkeley, California 94720, United States; McKetta Department of Chemical Engineering, University of Texas at Austin, Austin, Texas 78712, United States; [orcid.org/0000-0001-7311-7873](https://orcid.org/0000-0001-7311-7873)

Complete contact information is available at: <https://pubs.acs.org/doi/10.1021/acs.nanolett.0c02992>

### Notes

The authors declare no competing financial interest.

## ■ ACKNOWLEDGMENTS

This research was supported by the National Science Foundation (NSF), including CHE-1905263, NASCENT, an NSF ERC (EEC-1160494, C.M.S.), and a Graduate Research Fellowship under Award Number (DGE-1610403, S.L.G.). Additional support came from the Welch Foundation (F-1848).

## ■ REFERENCES

- (1) Mayer, K. M.; Hafner, J. H. Localized Surface Plasmon Resonance Sensors. *Chem. Rev.* **2011**, *111*, 3828–3857.
- (2) Akselrod, G. M.; Argyropoulos, C.; Hoang, T. B.; Ciraci, C.; Fang, C.; Huang, J.; Smith, D. R.; Mikkelsen, M. H. Probing the Mechanisms of Large Purcell Enhancement in Plasmonic Nano-antennas. *Nat. Photonics* **2014**, *8*, 835–840.
- (3) Deeb, C.; Zhou, X.; Plain, J.; Wiederrecht, G. P.; Bachelot, R.; Russell, M.; Jain, P. K. Size Dependence of the Plasmonic Near-Field

Measured via Single-Nanoparticle Photoimaging. *J. Phys. Chem. C* **2013**, *117*, 10669–10676.

(4) Hirsch, L. R.; Stafford, R. J.; Bankson, J. A.; Sershen, S. R.; Rivera, B.; Price, R. E.; Hazle, J. D.; Halas, N. J.; West, J. L. Nanoshell-Mediated near-Infrared Thermal Therapy of Tumors under Magnetic Resonance Guidance. *Proc. Natl. Acad. Sci. U. S. A.* **2003**, *100*, 13549–13554.

(5) Baffou, G.; Quidant, R. Thermo-Plasmonics: Using Metallic Nanostructures as Nano-Sources of Heat. *Laser Photonics Rev.* **2013**, *7*, 171–187.

(6) Brongersma, M. L.; Halas, N. J.; Nordlander, P. Plasmon-Induced Hot Carrier Science and Technology. *Nat. Nanotechnol.* **2015**, *10*, 25–34.

(7) Christopher, P.; Xin, H.; Linic, S. Visible-Light-Enhanced Catalytic Oxidation Reactions on Plasmonic Silver Nanostructures. *Nat. Chem.* **2011**, *3*, 467–472.

(8) Christopher, P.; Moskovits, M. Hot Charge Carrier Transmission from Plasmonic Nanostructures. *Annu. Rev. Phys. Chem.* **2017**, *68*, 379–398.

(9) Agrawal, A.; Cho, S. H.; Zandi, O.; Ghosh, S.; Johns, R. W.; Milliron, D. J. Localized Surface Plasmon Resonance in Semiconductor Nanocrystals. *Chem. Rev.* **2018**, *118*, 3121–3207.

(10) Agrawal, A.; Johns, R. W.; Milliron, D. J. Control of Localized Surface Plasmon Resonances in Metal Oxide Nanocrystals. *Annu. Rev. Mater. Res.* **2017**, *47*, 1–31.

(11) Della Gaspera, E.; Chesman, A. S. R.; van Embden, J.; Jasieniak, J. J. Non-Injection Synthesis of Doped Zinc Oxide Plasmonic Nanocrystals. *ACS Nano* **2014**, *8*, 9154–9163.

(12) Runnerstrom, E. L.; Bergerud, A.; Agrawal, A.; Johns, R. W.; Dahlman, C. J.; Singh, A.; Selbach, S. M.; Milliron, D. J. Defect Engineering in Plasmonic Metal Oxide Nanocrystals. *Nano Lett.* **2016**, *16*, 3390–3398.

(13) Agrawal, A.; Kriegel, I.; Milliron, D. J. Shape-Dependent Field Enhancement and Plasmon Resonance of Oxide Nanocrystals. *J. Phys. Chem. C* **2015**, *119*, 6227–6238.

(14) Crockett, B. M.; Jansons, A. W.; Koskela, K. M.; Johnson, D. W.; Hutchison, J. E. Radial Dopant Placement for Tuning Plasmonic Properties in Metal Oxide Nanocrystals. *ACS Nano* **2017**, *11*, 7719–7728.

(15) Lounis, S. D.; Runnerstrom, E. L.; Bergerud, A.; Nordlund, D.; Milliron, D. J. Influence of Dopant Distribution on the Plasmonic Properties of Indium Tin Oxide Nanocrystals. *J. Am. Chem. Soc.* **2014**, *136*, 7110–7116.

(16) Ito, D.; Yokoyama, S.; Zaikova, T.; Masuko, K.; Hutchison, J. E. Synthesis of Ligand-Stabilized Metal Oxide Nanocrystals and Epitaxial Core/Shell Nanocrystals via a Lower-Temperature Esterification Process. *ACS Nano* **2014**, *8*, 64–75.

(17) Jansons, A. W.; Hutchison, J. E. Continuous Growth of Metal Oxide Nanocrystals: Enhanced Control of Nanocrystal Size and Radial Dopant Distribution. *ACS Nano* **2016**, *10*, 6942–6951.

(18) Staller, C. M.; Robinson, Z. L.; Agrawal, A.; Gibbs, S. L.; Greenberg, B. L.; Lounis, S. D.; Kortshagen, U. R.; Milliron, D. J. Tuning Nanocrystal Surface Depletion by Controlling Dopant Distribution as a Route Toward Enhanced Film Conductivity. *Nano Lett.* **2018**, *18*, 2870–2878.

(19) Gibbs, S. L.; Staller, C. M.; Milliron, D. J. Surface Depletion Layers in Plasmonic Metal Oxide Nanocrystals. *Acc. Chem. Res.* **2019**, *52*, 2516–2524.

(20) Zhang, C.; Chen, B.-Q.; Li, Z.-Y.; Xia, Y.; Chen, Y.-G. Surface Plasmon Resonance in Bimetallic Core–Shell Nanoparticles. *J. Phys. Chem. C* **2015**, *119*, 16836–16845.

(21) Moskovits, M.; Srnová-Šloufová, I.; Vlčková, B. Bimetallic Ag–Au Nanoparticles: Extracting Meaningful Optical Constants from the Surface-Plasmon Extinction Spectrum. *J. Chem. Phys.* **2002**, *116*, 10435–10446.

(22) Lu, L.; Burkey, G.; Halaciuga, I.; Goia, D. V. Core–Shell Gold/Silver Nanoparticles: Synthesis and Optical Properties. *J. Colloid Interface Sci.* **2013**, *392*, 90–95.

- (23) Prodan, E.; Radloff, C.; Halas, N. J.; Nordlander, P. A Hybridization Model for the Plasmon Response of Complex Nanostructures. *Science* **2003**, *302*, 419–422.
- (24) Prodan, E.; Nordlander, P. Plasmon Hybridization in Spherical Nanoparticles. *J. Chem. Phys.* **2004**, *120*, 5444–5454.
- (25) Tandon, B.; Yadav, A.; Khurana, D.; Reddy, P.; Santra, P. K.; Nag, A. Size-Induced Enhancement of Carrier Density, LSPR Quality Factor, and Carrier Mobility in Cr–Sn Doped In<sub>2</sub>O<sub>3</sub> Nanocrystals. *Chem. Mater.* **2017**, *29*, 9360–9368.
- (26) Liu, Z.; Zhong, Y.; Shafei, I.; Jeong, S.; Wang, L.; Nguyen, H. T.; Sun, C.-J.; Li, T.; Chen, J.; Chen, L.; Losovyj, Y.; Gao, X.; Ma, W.; Ye, X. Broadband Tunable Mid-Infrared Plasmon Resonances in Cadmium Oxide Nanocrystals Induced by Size-Dependent Nonstoichiometry. *Nano Lett.* **2020**, *20*, 2821–2828.
- (27) Lounis, S. D.; Runnerstrom, E. L.; Llordés, A.; Milliron, D. J. Defect Chemistry and Plasmon Physics of Colloidal Metal Oxide Nanocrystals. *J. Phys. Chem. Lett.* **2014**, *5*, 1564–1574.
- (28) Hewitt, R. W.; Winograd, N. Oxidation of Polycrystalline Indium Studied by X-ray Photoelectron Spectroscopy and Static Secondary Ion Mass Spectroscopy. *J. Appl. Phys.* **1980**, *51*, 2620–2624.
- (29) Staller, C. M.; Gibbs, S. L.; Saez Cabezas, C. A.; Milliron, D. J. Quantitative Analysis of Extinction Coefficients of Tin-Doped Indium Oxide Nanocrystal Ensembles. *Nano Lett.* **2019**, *19*, 8149–8154.
- (30) Sihvola, A. *Electromagnetic Mixing Formulas and Applications*; The Institution of Electrical Engineers, 1999.
- (31) Zandi, O.; Agrawal, A.; Shearer, A. B.; Reimnitz, L. C.; Dahlman, C. J.; Staller, C. M.; Milliron, D. J. Impacts of Surface Depletion on the Plasmonic Properties of Doped Semiconductor Nanocrystals. *Nat. Mater.* **2018**, *17*, 710–717.
- (32) Whitney, A. V.; Elam, J. W.; Zou, S.; Zinovev, A. V.; Stair, P. C.; Schatz, G. C.; Van Duyne, R. P. Localized Surface Plasmon Resonance Nanosensor: A High-Resolution Distance-Dependence Study Using Atomic Layer Deposition. *J. Phys. Chem. B* **2005**, *109*, 20522–20528.
- (33) Haes, A. J.; Zou, S.; Schatz, G. C.; Van Duyne, R. P. Nanoscale Optical Biosensor: Short Range Distance Dependence of the Localized Surface Plasmon Resonance of Noble Metal Nanoparticles. *J. Phys. Chem. B* **2004**, *108*, 6961–6968.
- (34) Haes, A. J.; Zou, S.; Schatz, G. C.; Van Duyne, R. P. A Nanoscale Optical Biosensor: The Long Range Distance Dependence of the Localized Surface Plasmon Resonance of Noble Metal Nanoparticles. *J. Phys. Chem. B* **2004**, *108*, 109–116.
- (35) Neubrech, F.; Huck, C.; Weber, K.; Pucci, A.; Giessen, H. Surface-Enhanced Infrared Spectroscopy Using Resonant Nanoantennas. *Chem. Rev.* **2017**, *117*, 5110–5145.
- (36) Adato, R.; Aksu, S.; Altug, H. Engineering Mid-Infrared Nanoantennas for Surface Enhanced Infrared Absorption Spectroscopy. *Mater. Today* **2015**, *18*, 436–446.
- (37) Adato, R.; Altug, H. In-Situ Ultra-Sensitive Infrared Absorption Spectroscopy of Biomolecule Interactions in Real Time with Plasmonic Nanoantennas. *Nat. Commun.* **2013**, *4*, 2154.
- (38) Wu, C.; Khanikaev, A. B.; Adato, R.; Arju, N.; Yanik, A. A.; Altug, H.; Shvets, G. Fano-Resonant Asymmetric Metamaterials for Ultrasensitive Spectroscopy and Identification of Molecular Monolayers. *Nat. Mater.* **2012**, *11*, 69–75.
- (39) Cho, S. H.; Roccapriore, K. M.; Dass, C. K.; Ghosh, S.; Choi, J.; Noh, J.; Reimnitz, L. C.; Heo, S.; Kim, K.; Xie, K.; Korgel, B. A.; Li, X.; Hendrickson, J. R.; Hachtel, J. A.; Milliron, D. J. Spectrally Tunable Infrared Plasmonic F<sub>2</sub>Sn:In<sub>2</sub>O<sub>3</sub> Nanocrystal Cubes. *J. Chem. Phys.* **2020**, *152*, No. 014709.
- (40) Sönnichsen, C.; Reinhard, B. M.; Liphardt, J.; Alivisatos, A. P. A Molecular Ruler Based on Plasmon Coupling of Single Gold and Silver Nanoparticles. *Nat. Biotechnol.* **2005**, *23*, 741–745.
- (41) Jain, P. K.; El-Sayed, M. A. Universal Scaling of Plasmon Coupling in Metal Nanostructures: Extension from Particle Pairs to Nanoshells. *Nano Lett.* **2007**, *7*, 2854–2858.
- (42) Tandon, B.; Agrawal, A.; Heo, S.; Milliron, D. J. Competition between Depletion Effects and Coupling in the Plasmon Modulation of Doped Metal Oxide Nanocrystals. *Nano Lett.* **2019**, *19*, 2012–2019.
- (43) Agrawal, A.; Kriegel, I.; Runnerstrom, E. L.; Scotognella, F.; Llordés, A.; Milliron, D. J. Rationalizing the Impact of Surface Depletion on Electrochemical Modulation of Plasmon Resonance Absorption in Metal Oxide Nanocrystals. *ACS Photonics* **2018**, *5*, 2044–2050.
- (44) Mendelsberg, R. J.; Garcia, G.; Li, H.; Manna, L.; Milliron, D. J. Understanding the Plasmon Resonance in Ensembles of Degenerately Doped Semiconductor Nanocrystals. *J. Phys. Chem. C* **2012**, *116*, 12226–12231.
- (45) Johns, R. W.; Bechtel, H. A.; Runnerstrom, E. L.; Agrawal, A.; Lounis, S. D.; Milliron, D. J. Direct Observation of Narrow Mid-Infrared Plasmon Linewidths of Single Metal Oxide Nanocrystals. *Nat. Commun.* **2016**, *7*, 11583.
- (46) Sun, Y.; Xia, Y. Increased Sensitivity of Surface Plasmon Resonance of Gold Nanoshells Compared to That of Gold Solid Colloids in Response to Environmental Changes. *Anal. Chem.* **2002**, *74*, 5297–5305.
- (47) Giraldo, J. P.; Landry, M. P.; Kwak, S.-Y.; Jain, R. M.; Wong, M. H.; Iverson, N. M.; Ben-Naim, M.; Strano, M. S. A Ratiometric Sensor Using Single Chirality Near-Infrared Fluorescent Carbon Nanotubes: Application to In Vivo Monitoring. *Small* **2015**, *11*, 3973–3984.
- (48) Lv, X.; Liu, J.; Liu, Y.; Zhao, Y.; Sun, Y.-Q.; Wang, P.; Guo, W. Ratiometric Fluorescence Detection of Cyanide Based on a Hybrid Coumarin–Hemicyanine Dye: The Large Emission Shift and the High Selectivity. *Chem. Commun.* **2011**, *47*, 12843–12845.
- (49) Xing, P.; Xu, Y.; Li, H.; Liu, S.; Lu, A.; Sun, S. Ratiometric and Colorimetric Near-Infrared Sensors for Multi-Channel Detection of Cyanide Ion and Their Application to Measure  $\beta$ -Glucosidase. *Sci. Rep.* **2015**, *5*, 1–6.
- (50) Zhao, Q.; Zhao, T.; Guo, J.; Chen, W.; Zhang, M.; Kagan, C. R. The Effect of Dielectric Environment on Doping Efficiency in Colloidal PbSe Nanostructures. *ACS Nano* **2018**, *12*, 1313–1320.
- (51) Runnerstrom, E. L.; Kelley, K. P.; Folland, T. G.; Nolen, J. R.; Engheta, N.; Caldwell, J. D.; Maria, J.-P. Polaritonic Hybrid-Epsilon-near-Zero Modes: Beating the Plasmonic Confinement vs Propagation-Length Trade-Off with Doped Cadmium Oxide Bilayers. *Nano Lett.* **2019**, *19*, 948–957.
- (52) Oulton, R. F.; Sorger, V. J.; Genov, D. A.; Pile, D. F. P.; Zhang, X. A Hybrid Plasmonic Waveguide for Subwavelength Confinement and Long-Range Propagation. *Nat. Photonics* **2008**, *2*, 496–500.
- (53) Linic, S.; Christopher, P.; Ingram, D. B. Plasmonic-Metal Nanostructures for Efficient Conversion of Solar to Chemical Energy. *Nat. Mater.* **2011**, *10*, 911–921.
- (54) Li, K.; Hogan, N. J.; Kale, M. J.; Halas, N. J.; Nordlander, P.; Christopher, P. Balancing Near-Field Enhancement, Absorption, and Scattering for Effective Antenna–Reactor Plasmonic Photocatalysis. *Nano Lett.* **2017**, *17*, 3710–3717.
- (55) Aslam, U.; Rao, V. G.; Chavez, S.; Linic, S. Catalytic Conversion of Solar to Chemical Energy on Plasmonic Metal Nanostructures. *Nat. Catal.* **2018**, *1*, 656.
- (56) Zhou, L.; Swearer, D. F.; Zhang, C.; Robotjazi, H.; Zhao, H.; Henderson, L.; Dong, L.; Christopher, P.; Carter, E. A.; Nordlander, P.; Halas, N. J. Quantifying Hot Carrier and Thermal Contributions in Plasmonic Photocatalysis. *Science* **2018**, *362*, 69–72.
- (57) Link, S.; El-Sayed, M. A. Spectral Properties and Relaxation Dynamics of Surface Plasmon Electronic Oscillations in Gold and Silver Nanodots and Nanorods. *J. Phys. Chem. B* **1999**, *103*, 8410–8426.
- (58) Johns, R. W.; Blemker, M. A.; Azzaro, M. S.; Heo, S.; Runnerstrom, E. L.; Milliron, D. J.; Roberts, S. T. Charge Carrier Concentration Dependence of Ultrafast Plasmonic Relaxation in Conducting Metal Oxide Nanocrystals. *J. Mater. Chem. C* **2017**, *5*, 5757–5763.